Supplemental Material

Imprinting persistent currents in tunable fermionic rings

G. Del Pace,[1,*] K. Xhani,[1] A. Muzi Falconi,[2,1] M. Fedrizzi,[1] N. Grani,[1]
D. Hernandez Rajkov,[1] M. Inguscio,[3,1] F. Scazza,[2,1] W. J. Kwon,[1,†] and G. Roati[1]

[1]*Istituto Nazionale di Ottica del Consiglio Nazionale delle Ricerche (CNR-INO) and European Laboratory for Nonlinear Spectroscopy (LENS), University of Florence, 50019 Sesto Fiorentino, Italy*
[2]*Department of Physics, University of Trieste, 34127 Trieste, Italy*
[3]*Department of Engineering, Campus Bio-Medico University of Rome, 00128 Rome, Italy*

S.1. EXTRACTING LOCAL INFORMATION FROM INTERFERENCE PATTERNS

In this section we provide further information about the local fitting of the interferograms presented in the main text. As the interference fringes have a high contrast in the BEC regime, to probe the winding number of UFG and BCS superfluids we acquire the interferograms after adiabatically sweeping the s-wave scattering length to the BEC regime with a $50\,$ms ramp before performing a time-of-flight (TOF) expansion. Thanks to the high resolution $\sim 1\,\mu$m of our imaging system, we are able to measure the relative phase ϕ locally, with an azimuthal angular resolution of a few degrees. For this, we apply the following fitting procedure to the interferograms. We start by transforming the images from cartesian to polar coordinates, obtaining the interference pattern optical density I as a function of the azimuthal angle θ and the radial position r [see Fig. S1(b)]. We then cut the $I(\theta, r)$ profile into slices at fixed θ, and fit each $I(r)$ profile with a cosine multiplied by a Gaussian function [see Fig. S1(c)]. The phase of each fitted cosine function allows to extract the local phase difference $\phi(\theta)$ between the reference disk and the ring. By performing a linear fit of $\phi(\theta)$ we extract the winding number w [see Fig. S1(d) and fitted w values in the caption]. We verified that the described fitting procedure is applicable for any value of w obtained in the experiments, although it becomes less reliable for $w \gtrsim 5$ due to the more complex pattern characterizing the interferograms.

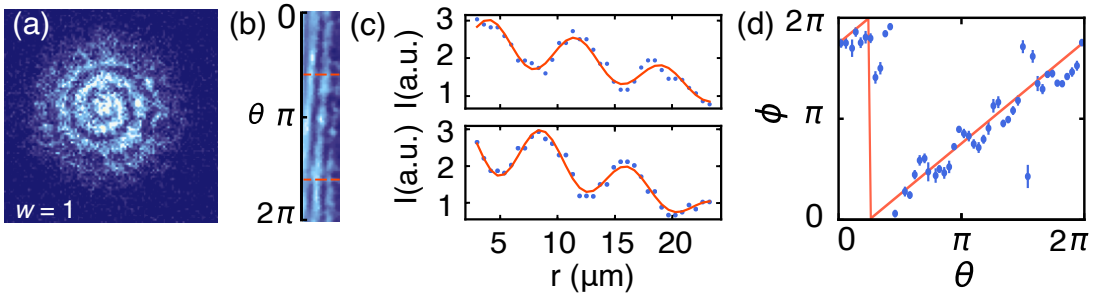

FIG. S1. Fitting procedure of the local phase $\phi(\theta)$. The acquired interferogram (a) is converted into polar coordinates, and a region of $1.5\,\mu$m $< r < 12\,\mu$m is selected (b). The $I(r, \theta)$ profile is sliced into 100 strips, centred around a given azimuthal angle, and then fitted with a cosine function multiplied by a Gaussian envelope to extract the local phase shift $\phi(\theta)$ (c). The resulting $\phi(\theta)$ profile is fitted with a line to extract the winding number w as slope (d), obtaining $w = 1.00(9)$. Symbols (errorbars) in panel (d) represents the weighted average (weighted standard deviation) over the fitted values of ϕ and their 1σ uncertainty in bins of $0.125\,$rad size.

* Present address: Institute of Physics, EPFL, 1015 Lausanne, Switzerland; E-mail: delpace@lens.unifi.it
† Present address: Department of Physics, Ulsan National Institute of Science and Technology (UNIST), Ulsan 44919, Republic of Korea

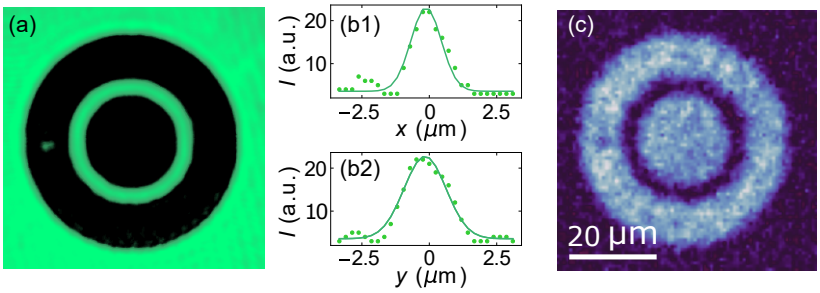

FIG. S2. Local defect characterization. (a) Image of the DMD pattern employed to introduce the small obstacle, visible as a small defect on the left side of the ring. (b1-2) Gaussian fit of the obstacle intensity profile I along the $x-y$ direction. (c) *In situ* image of a molecular BEC ring in presence of the local defect. The image is obtained as a single absorption image of the experimental sample.

S.2. OBSTACLE CHARACTERIZATION

We characterize the small obstacle employed in Sec. V of the main text by projecting the DMD-created image on a CCD camera [Fig. S2(a)] [1]. We perform a two-dimensional Gaussian fit of the obstacle intensity profile, finding that is has an approximately round profile of full width at half maximum (FWHM) of $1.6\,\mu$m [Figs. S2(b1),(b2)], which is comparable with the characteristic correlation length of the investigated superfluids. From the amplitude of the fitted Gaussian profile we extract the potential height V_0, which is calibrated by employing the procedure described in Ref. 1. The small size of the obstacle and the limited signal-to-noise ratio of CCD images make the calibration of V_0 not particularly precise. The obstacle height is adjusted to the value of $V_0/E_F \approx 0.1$ for the BEC superfluid, and to $V_0/E_F \approx 0.2$ for UFG and BCS ones by tuning the green light power impinging on the DMD. The obstacle height rescaled to the chemical potential in each regime is $V_0/\mu \simeq \{0.85,\, 0.19,\, 0.23\}$ for BEC, unitary and BCS superfluid, respectively. Figure S2(c) shows the *in situ* image of molecular BEC superfluid in presence of the local defect: the hole in the density produced by the latter confirms that $V_0/\mu \approx 1$.

The same potential height calibration is used to measure the light shift U_0 induced by the light gradient employed in the imprinting procedure. With this knowledge, we compute the imprinted phase as $\Delta\phi_I = U_0 \times t_I/\hbar$, where t_I is the imprinting time. The error associated to this quantity in all figures corresponds to the 5% uncertainty on the calibration of U_0.

S.3. MAXIMUM WINDING NUMBER STATE

By increasing the time duration of the imprinting pulse we are able to excite states with increasing winding number w, as reported in Fig. S3(a). While for the shorter imprinting times we clearly observe a step-like profile of the populated circulation states, this profile becomes linear as we increase the imprinted phase jump. This washing-out of the steps profile reflects the lower reliability of the imprinting procedure for the highest circulation states. We investigate the fidelity of our imprinting procedure for the $w = 1$ state by acquiring more than 100 interferograms and evaluating the winding number for each of them. We estimate that the probability of populating the $w = 1$ circulation state is $> 99\%$ in the BEC and UFG regimes and a few percent lower in the BCS. This value decreases significantly if the imprinting time is increased, with w displaying significant shot-to-shot fluctuations. In particular, we find that the maximum circulation state attainable with a single imprinting pulse of large $\Delta\phi_I$ is $w = 6$ in all three superfluid regimes. We ascribe this to the density excitations caused by the imprinting procedure, which become more dramatic for larger t_I and could favour the entrance of vortices from the inner ring radius, effectively lowering the winding number in the ring. As described in the main text, we thus typically employ multiple short imprinting pulses of $t_I \lesssim 200\,\mu$s to achieve the highest fidelity for exciting large-w states.

Disregarding the short timescale phenomena described in the previous section, we find that for all $1 \geq w \geq w_{\text{max}}$ states the current is stable over timescales longer than that required to complete one entire loop around the ring. In particular, we find $w_{\text{max}} = \{8,\, 9,\, 6\}$ in the BEC, UFG and BCS regimes, respectively. Higher circulations $w > w_{\text{max}}$ are also accessible, but they

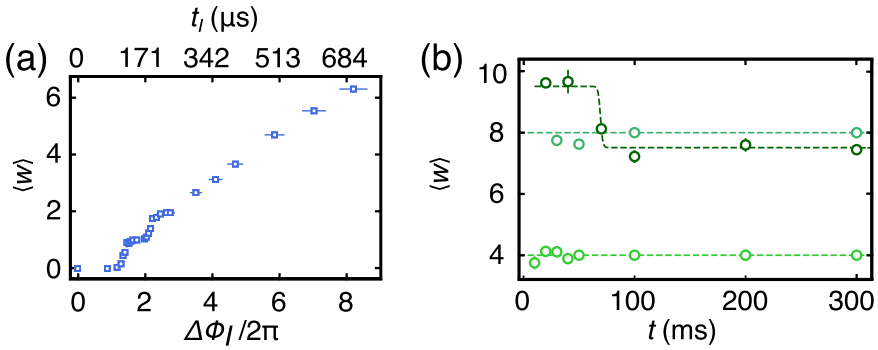

FIG. S3. (a) Average winding number as a function of the imprinted phase jump (lower x-axis) and the imprinting time (upper x-axis) in the unitary regime. Each point corresponds to the average of ~ 15 experimental repetitions. Vertical error bars denote the standard deviation of the mean, horizontal ones are related only to the lower x-axis and are obtained considering the experimental uncertainty of $\sim 5\%$ in the U_0 calibration. (b) Time evolution of higher winding number in the BEC regime. The maximum stable circulation state that we can observe is $w = 8$, while higher w states decay back to this value. Each point corresponds to ~ 15 experimental data points, error bars are the standard deviation of the mean. The dark green dashed line represents a sigmoidal fit of the data at $\langle w_0 \rangle \simeq 10$, lighter green lines correspond to $\langle w \rangle = 8, 4$.

decay to lower values over timescales comparable with a few round trip times, which is roughly 40 ms for $w = 8$ [see Fig. S3(b)]. At unitarity, to avoid the current decay during the magnetic field ramp of 50 ms necessary to observe the interferograms in the strongly-interacting regime, we probe the states at $w > 8$, i.e. w_{max} in the BEC regime, with a different detection protocol. We employ a fast magnetic field ramp of 3.8 ms, timed such that during its last 1.3 ms the atomic cloud perform a free TOF expansion. With such a detection protocol, the current at $w = 9$ is observed to persist for at leat 400 ms, whereas the one at $w = 10$ shows a similar decay to that plotted in Fig. S3(b). We have checked that for currents at $w \leq 8$, the sweep duration does not affect the interferograms, as in this regime the critical current of the BEC superfluid is never exceeded. For all the investigated currents in the BCS regime, we employ the 50 ms ramp, since w_{max} in this regime is lower than in the BEC one, and longer sweeps provide higher contrast of the interferograms. Consistently with our interpretation of w_{max} as related to the current velocity at the inner ring radius exceeding the critical velocity for vortex nucleation, we have verified that the maximum winding strikingly depends on R_{in}, whereas it is completely unaffected by a change of R_{out} as long as the ring thickness is kept larger than $\simeq 5\,\mu$m. For thinner rings we observe progressively lower w_{max} for a given R_{in}, most likely due to a more dramatic effect of the density excitations introduced by the phase imprinting, which could be more stable in more tightly confined geometries.

THEORETICAL DESCRIPTION

A. GPE simulations of the experimental imprinting procedure

The theoretical study in the BEC limit is performed at $T = 0$ by numerically solving the time-dependent mean-field 3D Gross-Pitaevskii Equation (GPE):

$$i\hbar\frac{\partial\Psi(\mathbf{r},t)}{\partial t} = -\frac{\hbar^2}{2M}\nabla^2\Psi(\mathbf{r},t) + V\Psi(\mathbf{r},t) + g|\Psi(\mathbf{r},t)|^2\Psi(\mathbf{r},t) \tag{S.1}$$

where $\Psi(\mathbf{r},t)$ is the condensate wave function, $M = 2\,m$ the molecular mass, V the external trapping potential, $g = 4\pi\hbar^2 a_M/M$ is the interaction strength with $a_M = 0.6a = 53.3$ nm the molecular scattering length. In our study, we employ a ring-trap geometry with hard-wall boundaries such that the external potential is defined as follows:

$$V = \frac{1}{2}M\left(\omega_\perp^2 r^2 + \omega_z^2 z^2\right) + V_{\text{ring}} \quad , \tag{S.2}$$

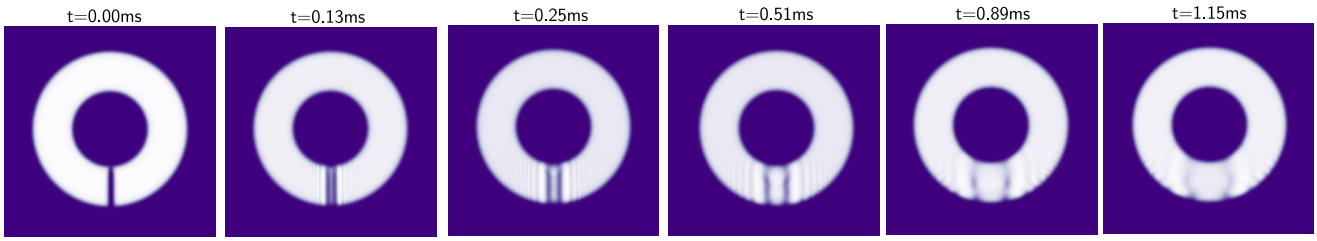

FIG. S4. Short-time evolution of the 2D density along the $x-y$ plane at $z=0$ showing the decay of the density depletion for an imprinted phase $\Delta\phi_I = 2\pi$.

where $\{\omega_\perp,\, \omega_z\} = 2\pi \times \{2.5\,,\, 396\}$ Hz are the radial and axial trapping frequencies, respectively, and

$$V_{\rm ring} = V_1\left[\tanh\left(\frac{r-R_{out}}{d}\right)+1\right] + V_1\left[\tanh\left(\frac{R_{\rm in}-r}{d}\right)+1\right]. \tag{S.3}$$

The parameters of $V_{\rm ring}$ are chosen such that the numerical density matches the experimental one, i.e. $\{R_{\rm in},\, R_{\rm out}\} = \{9.6\,,\, 21.0\}\,\mu$m and $d = 0.37\,\mu$m, while $V_1 = 2.5\,\mu$ is chosen to be larger than the chemical potential μ so the density goes to zero at the boundary. For a particle number equal to the experimental one $N = 7.5\times10^3$, we numerically obtain $\mu = 1.06$ kHz and a healing length of $\xi = 0.61\,\mu m$, consistent with the calculated ones for the experimental BEc superfluid.

Equation S.1 is solved numerically on a Cartesian grid of $\{N_x, N_y, N_z\} = \{256, 256, 80\}$ points along x, y, and z direction, respectively. We use a grid size of the same length in the radial plane, i.e. $-34.846\,\mu{\rm m} \le x, y \le 34.846\,\mu$m and $-11.0\,\mu{\rm m} \le z \le 11.0\,\mu$m. This gives rise to a grid spacing along the three directions of $\Delta x = \Delta y = 0.45\,\xi$ and $\Delta z = 0.46\,\xi$. The time step is instead set to $\Delta t = 1\times10^{-5}\,\omega_\perp^{-1}$.

The ground state wavefunction is found by solving the GPE in imaginary time. We then imprint a phase $\Delta\phi_I(\theta) = U(\theta)t_I/\hbar$ on the initial condensate wavefunction, for a given imprinting time t_I. In order to model the experimental imprinting potential shown in Fig. 2 of the main text, the imprinted function $U(\theta)$ is chosen to be a decreasing function of the azimuthal angle θ in the range $[0, 2\pi-\Delta\theta]$ starting from $U(\theta) = U_0$ at $\theta = 0$ and reaching the zero value for $\theta = 2\pi - \Delta\theta$. Then it turns back to the initial value in $\Delta\theta = 0.15$ rad. The presence of this opposite-sign gradient leads the superfluid density to present a cut after the imprinting, as shown in Fig. S4(a1). This density depletion quickly decays over a few ms timescale into sound waves for $\Delta\phi_I/2\pi < 4$ [Fig. S4], which does not affect the imprinted current. On the other hand, for $\Delta\phi_I/2\pi \ge 4$ the density excitations introduced by the imprinting give rise to vortices close to the inner radius of the ring, that initially perturb the current and then survive on top of it for long time. Furthermore, for $w_0 \ge 7$, the density excitation favours the vortex emission from the inner ring radius, setting the effective limit of w reachable with a single imprinting pulse. This is consistent with the experimental findings of $w_{\rm max} = 6$ for a single imprinting pulse, as discussed in the main and in the previous section.

In order to directly compare our numerical data with the experimental one, we employ the same interferometric technique for extracting the persistent current winding number. As described in the main, it consists on adding a central disc condensate as phase reference and acquiring the interference pattern arising after a TOF expansion. In order to do so, in our simulations we separate the ring from the disc by implementing a circular Gaussian barrier and changing $V_{\rm ring}$ of Eq. S.3 to:

$$V_{\rm ring} = V_1\left[\tanh\left(\frac{r-R_{\rm out}}{d}\right)+1\right] + V_1\exp\left[-\frac{2(R_{\rm in}-r)^2}{d^2}\right]. \tag{S.4}$$

where $d = 1.1\,\mu$m. The total number of pair considerend in the whole trap is now 10×10^3. To obtain the interferograms, we remove $V_{\rm ring}$ in 0.3 ms, while keeping the harmonic vertical confinement. As the superfluid expands in the $x-y$ plane during the TOF, we modify accordingly the numerical grid to contain it all while keeping the same grid spacing as for the simple ring simulations. Thus, we modify our grid size by taking the number of grid points to be $N_x = N_y = 384$ for a grid size of length $53.186\mu{\rm m} \le x, y \le 53.186\mu$m, keeping so the grid spacing equal to the case where only ring superfluid is present.

B. Numerical simulations of the persistent current decay

The experimental studies of the decay of the persistent current in the presence of the defect are performed after the density depletion has already decayed. For this reason and in order to focus only in the effect of the defect on the supercurrent decay, in our numerical simulations of this part we simply imprint a phase in the initial condensate density, i.e. without including the antigradient potential. In this way no density excitations perturb the superfluid initially. Moreover, the experiment is performed at finite temperature which means that the system is composed of condensate and thermal particles. The experimental condensed fraction decreases from 85% before the imprinting to 80% at the end of the time evolution in the presence of the defect. These values of condensed fraction are measured in the harmonic trap before lading the ring potential in the $x-y$ plane. For the numerical study of the current decay we thus consider a number of particles equal to the 80% of the total experimental 7.5×10^3 pairs, as with GPE only the condensate dynamic is taken into account. By employing the collisionless Zaremba-Nikuni-Griffin model [2], we have numerically checked that at the experimental temperature of $T=0.4\,T_c$ and same condensate number [3], the presence of a thermal cloud does not affect the critical winding w_c, but it rather alters both Γ and w_F.

Also in this study, we initially investigate the ring superfluid only to describe the microscopic mechanism of vortex emission. Under these conditions, we extract the local superfluid velocity and the local speed of sound, as discussed in Appendix B of the main text. We then turn to the composite geometry including the disc condensate, in order to extract information about the winding number w from the interferograms. We note that the experimental inner and outer ring radius in the presence of the inner disc are slightly different with respect to the simple ring, which give rise to smoother boundary conditions. For this reason we slightly change the parameters of $V_{\rm ring}$ of Eq. S.4 by employing $\{R_1,\,R_2\}=\{10.2\,,\,20.6\}\,\mu$m and $d=1.46\,\mu$m. With these new parameters the new chemical potential increases to $\mu=1.13$ kHz. The defect is parametrized with the following Gaussian shape:

$$V_{\rm defect}=V_0\exp\left[-\frac{2(x-x_0)^2}{\sigma^2}\right]\exp\left[-\frac{2y^2}{\sigma^2}\right], \tag{S.5}$$

with $x_0=-15.0\,\mu$m, $\sigma=1.4\,\mu$m and $V_0=0.96\,\mu$. The studies performed in the superfluid ring with or without the inner disk condensate show a small shift on the timing of vortex nucleation, due to differences in the boundary conditions, but they display the same number of emitted vortices and the same critical circulation w_c.

C. Thermodynamic properties of the superfluids throughout the BEC-BCS crossover

In order to evaluate the thermodynamic properties of the superfluids in a unified manner throughout the BEC-BCS crossover, we exploit the polytropic approximation for a trapped gas, where the effective polytropic index $\gamma=\partial\log\mu/\partial\log n$ leads to the power-law relation $\mu\propto n^\gamma$ [4, 5]. In the BEC-limit, $\gamma=1$, while at unitarity and in the BCS-limit, $\gamma=2/3$. The polytropic approximation enables us to evaluate analytically μ and E_F of the crossover superfluids when neglecting the shallow harmonic confinement in the radial direction and considering a hard-wall potential in the plane. These approximations are sustained by the fact that the radial Thomas-Fermi radius provided by the 2.5 Hz harmonic trap in this direction is smaller than $R_{\rm out}$ and that the size of the box walls d is comparable with the characteristic length of the superfluid in each regime. We verified that such approximation provides results in agreement within 1% with the ones derived by accounting for the full trapping potential, i.e. by including also the radial harmonic confinement.

Under local density approximation, the Thomas-Fermi density profile is given by:

$$n(r,z)=\left(\frac{\mu_0}{g_\gamma}\right)^{1/\gamma}\left[1-\frac{z^2}{R_z^2}-\tilde{V}_{\rm ring}(r)\right]^{1/\gamma} \tag{S.6}$$

where R_z (R_r) are the Thomas-Fermi radius along the vertical (radial) direction, and $\tilde{V}_{\rm ring}(r)$ describe the hard wall potential:

$$\tilde{V}_{\rm ring}(r)=\begin{cases}0 & \text{for } R_{\rm in}<r<R_{\rm out},\\ \infty & \text{otherwise,}\end{cases} \tag{S.7}$$

where $R_{\rm in}$ and $R_{\rm out}$ are the internal and external ring radii. We integrate the density of Eq. (S.6) to obtain the total number of pairs N and to calculate the corresponding chemical potential that reads:

$$\mu_0 = \left[\frac{\Gamma(\frac{1}{\gamma}+\frac{3}{2})}{\pi^{3/2}\Gamma(\frac{1}{\gamma}+1)} \frac{\sqrt{M/2}\omega_z N g_\gamma^{1/\gamma}}{R_{\rm out}^2 - R_{\rm in}^2} \right]^{\frac{2\gamma}{\gamma+2}}, \tag{S.8}$$

where Γ is the Gamma function and g_γ is a prefactor that depends on the interaction limit: $g_{\rm BEC} = 4\pi\hbar^2 a_M/M$ with $a_M = 0.6\,a$ and $M = 2\,m$ for $(k_F a)^{-1} > 1$, $g_{\rm BCS} = \frac{\hbar^2}{2m}(6\pi^2)^{2/3}$ for $(k_F a_s)^{-1} < -1$ and $g_{\rm UFG} = \xi\frac{\hbar^2}{2m}(6\pi^2)^{2/3}$ for $-1 < (k_F a_s)^{-1} < 1$, where ξ is the Bertsch parameter taking the value of 0.37 at unitarity at $T = 0$ [5]. Similarly, from the density of Eq. (S.6) we calculate the Fermi energy:

$$E_F = 2\hbar \left[\frac{\hbar\omega_z N}{m(R_{\rm out}^2 - R_{\rm in}^2)} \right]^{1/2} \tag{S.9}$$

We apply the aforementioned relations to calculate E_F, μ and the speed of sound $c_s = \sqrt{\gamma\mu/m}$ for the three interaction regimes explored in this work, as reported in the main text. In particular, given the molecular nature of the BEC superfluid, we employ $M = 2\,m$ for the sound speed calculation, yielding μ and c_s values consistent with the results of the numerical simulation. On the other hand, given the small $|1/k_F a|$ value of the BCS superfluid, we calculate μ and c_s in this regime by assuming the expression at unitarity to be valid in the strongly interacting regime of $|1/k_F a| < 1$ and employing the Luttinger-Ward calculations across the BEC-BCS crossover of Ref. 6 at $1/k_F a = -0.4$ [1].

[1] W. J. Kwon, G. Del Pace, R. Panza, M. Inguscio, W. Zwerger, M. Zaccanti, F. Scazza, and G. Roati, *Strongly correlated superfluid order parameters from dc Josephson supercurrents*, Science **369**, 84 (2020).

[2] A. Griffin, T. Nikuni, and E. Zaremba, *Bose-Condensed Gases at Finite Temperatures* (Cambridge University Press, 2009).

[3] K. Xhani and N. P. Proukakis, *Dissipation in a finite-temperature atomic Josephson junction*, Phys. Rev. Research **4**, 033205 (2022).

[4] H. Heiselberg, *Collective Modes of Trapped Gases at the BEC-BCS Crossover*, Phys. Rev. Lett. **93**, 040402 (2004).

[5] R. Haussmann and W. Zwerger, *Thermodynamics of a trapped unitary Fermi gas*, Phys. Rev. A **78**, 063602 (2008).

[6] R. Haussmann, W. Rantner, S. Cerrito, and W. Zwerger, *Thermodynamics of the BCS-BEC crossover*, Phys. Rev. A **75**, 023610 (2007).